Heuristical Cone Beam Computed Optics

Jean-Baptiste Bellet, Gérard Berginc

Heuristical Cone Beam Computed Optics

Jean-Baptiste Bellet* and Gérard Berginc†

September 19, 2016‡

Abstract

Imaging a three-dimensional scene from a set of optical data is crucial for many applications, and is still an academical challenge. A new high-performant heuristic is emerging to solve this problem, from a set of cone beam reflective projections. The basis is visualizing appropriately a 3D heuristical reconstruction. The reconstruction step is the so-called reflective tomography: it rests on the filtered backprojection from Computed Tomography. The visualization step is based on volume rendering: the Maximum Intensity Projection. Combining these two steps is an original computational method to get new images of the initial reflective scene. Several questions concerning the validity of this new heuristic have emerged. Giving a mathematical meaning to the filtered backprojection of reflective projections is an open problem. Also controlling quantitatively the reconstruction and the obtained renderings has never been done. To answer such questions, we propose a new mathematical framework for the description of reflective tomography, and we design new criterions to check the amount of true informations in the renderings. We illustrate several properties of the method, by the means of a wide variety of numerical tests, including a real case. We show in particular that the images generated by the process are contrasted representations of the surfaces of the initial scene. This paper validates reflective tomography and the full heuristic as general compututational imaging methods. The main perspective is the design of a device for real-time high-resolution 3D imaging in optics, useful for the recognition of occluded objects emitting countermeasurements.

Keywords. 3D imaging, inverse optics, phaseless imaging, tomography, 3D visualization, Maximum Intensity Projection

1 Introduction

There is a considerable interest in the development of new optical imaging systems that are able to give three-dimensional images. Potential applications range across the field of defense and security for the recognition of targets, the medical field for the detection of subcutaneous and cutaneous tumors or the archaeological field for the discovery of remains in forests. The recognition is often performed by an operator who would like at the end to observe the objects of the considered scene, under the form of contrasted 2D images. A 3D technology offers more possibilities than a 2D one: the operator can simulate new views of the scene, he can move as a virtual observer inside the virtualized scene, he can select regions of interest and remove obstacles. Mapping a set of 2D optical images on new views of the scene with the ability to remove occlusions is still a very challenging task.

We and our co-authors are working on a new technology, designed to give a new answer to this challenge [4, 5, 7]. This technology is based on an active laser acquisition and on a mathematical heuristic. The device illuminates the scene with a laser (1.54 μm) and records a 2D image of backscattered intensities, for several angles of views. Such a record has several interesting properties. The illumination is eye-safe and non-ionizing. High-resolution images are considered. The

*J.-B. Bellet is with Université de Lorraine and CNRS, Institut Elie Cartan de Lorraine, UMR 7502, Metz, F-57045, France.

†G. Berginc is with Thales Optronique, 2, Avenue Gay Lussac CS 90502, 78995 Élancourt Cedex, France.

‡Version v6.4

active device changes the shadows when the angle of view changes. The acquisition can be fast and can be performed under several conditions, including night. The records are then processed by a mathematical heuristic. In this paper we focus on this heuristic. The heuristic has two steps. The first step computes a 3D reconstruction. Solving an appropriated inverse problem is unaffordable; the forward problem is itself very hard: multi-scales problems, including scattering by rough surfaces. So the approach is based on a heuristic: the reconstruction is computed by a filtered backprojection algorithm. This step is called reflective tomography, because an algorithm from Computed Tomography is used heuristically in order to invert reflective-kind measurements. This concept was introduced for several kinds of reflective experiments at the end of the 80's [15]. In our case we apply the Feldkamp Davis and Kress (FDK) algorithm [12] on a laser dataset [6, 8–10, 19]. This method appears numerically relevant to generate surfacic reconstruction of occluded objects, even from noisy datasets. The results for occluded opaque objects suggest also that the method works for incomplete data, such as limited-angle problems. The extracted surfaces may eventually need completion algorithms [3] for improving surface renderings. To get an alternative method of exploration of the reconstruction which goes further, we proposed very recently to directly visualize the reconstructed volume with a volume rendering method [1]. This step defines the second step of the global heuristic. We empirically observe that the surfaces of the original scene are located near the highest values of the reconstruction. That is the reason why we propose to use the Maximum Intensity Projection (MIP), which projects the volume by selection of the most intense voxel, along rays of projection. The combination of these two steps of reconstruction-visualization defines a global heuristic which answers to the proposed challenge.

This heuristic is an original computational method for 3D optical imaging. The steps are individually classical in other fields, but their combination in the field of interest is new. It is a direct (non-iterative) method and it can be performed automatically. The method can furthermore take benefit from the already known advantages of the individual steps. The FDK algorithm is very famous in Cone Beam Computed Tomography, for transmission by X-Ray. Several studies concern efficient implementations of such a filtered backprojection method, including implementations on Graphics Processing Unit (GPU) [13, 18, 21, 22, 26]. They enable fast reconstructions. Concerning the visualization part, the Maximum Intensity Projection is well known for medical applications [14,16,24,25]. Efficient implementations are available, for instance by using GPU or multi-resolution algorithms [11,20,27]. They enable a real-time interactive display. The proposed heuristic inherits of such capabilities: we show in [1] that we get at the end an interactive method, enabling displacements in the reconstructed scene, extraction of sub-volumes, and adjustement of the rendering.

In this paper, we would like to tackle some open questions about this new heuristic. They are mainly related to mathematical or quantitative validation of the approach. Indeed the standard mathematical result states that the filtered backprojection inverts the Radon transform; that is the justification of transmission tomography for complete data (knowledge of the full Radon transform). It is also known in this field that serious difficulties appear for incomplete data (*e.g.* limited angle problems), such as instabilities, or lack of reconstruction algorithms [17]. In reflective tomography, a filtered backprojection algorithm is applied on data which are not modelled by a Radon transform, and which are incomplete. Giving a mathematical framework and a meaning for such a reconstruction is a gap to be filled. By the way it is observed empirically that it provides relevant representations of the initial scene, for several physical configurations: measurements of travel-times or of backscattered intensities for example. So we would like a general mathematical model which includes both configurations.

Then as it is often the case in mathematical imaging, one of the main questions that arise for the validation of the process is the following: what is the error between the reconstruction and the original scene? Here this question is difficult, since the heuristical reconstruction is not supposed to represent some physical property of the scene. So we must before define criterions of quality to validate the process. The global process has a second step which produces images; they are supposed to be images of the scene. We would like to know if these images give nice visual perceptions of the original scene, and if they are accurate representations. Here again this validation is not obvious and criterions must be defined. Once criterions are defined, we would like to observe the kind of

numerical results that we get, and the behavior of the result when some parameters change. We would like to observe the key contributions that arise in the mathematical formulation. In order to check that the method is general, we would like to observe the result for several forward physical models. By the way a method must be stable to be useful in practice: a small perturbation of the input must produce a small perturbation on the output; so we need to check how the method deals with noise. And the last question is about the resolution. The output of the heuristic is wished to be sharper and sharper when the resolution of the input increases. We must check that point.

We answer to the previous questions in the following way. We start by describing 3D reflective tomography in a new and general manner; this extends the note [2] to 3D. We define a mathematical model, describing a general notion of reflective projection for a scene of opaque objects. Basically it considers cone beam projections; along each ray of projection, the model states that we measure an information concerning the first surfacic point of the scene which belongs to the ray. We do not assume any model for these informations; they could represent any physical information. Also a visible point of the scene can eventually be seen with different values for different angles of view. Then we briefly recall the FDK algorithm, and we identify in the reconstruction two components, explained by the discontinuities and the smooth parts of the input images. A discussion tends to reveal that "the reflective tomography combines the coherent horizontal contrasts at their true location in space". This interpretation links the reconstruction with the contrasts of the recorded images; it reveals that it is a far-reaching method, exactly as computing the gradient of a 2D image is a general way of contour detection. Then we discuss 3D visualization of a reconstruction in reflective tomography, especially by MIP. To the best of our knowledges, it is the most efficient way of extracting surfaces in that context, with the best resolution possible, and with a denoiser implicitely contained in the method. We describe MIP and how using this process as the visual field of a virtual observer, by considering cone beam projections; there is another originality here, since classical MIP uses orthographic projections. We include in the process the choice of the colormap, since it has a significative influence on the final visual perception. In a word we have the description of a new computational process which transforms a set of reflective cone-beam projections on new cone-beam projections, where we can remove occlusions. Despite we do not have mathematical theorems (very hard), we have at least intuitive explanations which motivate this heuristic.

Concerning the validation, we first propose to validate visually the reconstruction composed with the visualization. The visual perception that we get is indeed the first point to control; as usual in image processing, the visual aspect of the renderings is the main criterion of quality: the very first goal is producing images that can be appreciated by the human eye. This first stage is a quality control of the full process, which also implicitely controls the recontruction step. By the way, despite quantitative criterions do not necessarly reveal the feeling of the eye, they may be needed for objectivity. So we also define such objective criterions. In practice we interpret an output image as a contrasted image of the surfaces of the original scene; we would like to check that this interpretation is right. So we propose criterions based on the pixels in the output, that correspond really to surfacic points of the initial scene. For synthetic tests, these pixels can be discriminated because we know the original surfaces, and the pixels of the output represent voxels of the reconstructed volume. The proposed criterions are based on counting these surfacic pixels, and the proportion of intensity that they represent in the image. The same analysis is done for the other pixels, and several ratios can be computed. The main idea behind these criterions is estimating the level of *true* information in an output image. It is an original way of validating the full heuristic. We have even better: this way of validation aims at showing that MIP of the reconstruction selects surfacic points; so this also controls that the most intense values of the reconstruction are located near the initial surfaces. Thus this validates at the same time reflective tomography; this is the first time that reflective tomography is checked from this point of view. By the way this is also an original study concerning the true information of a MIP; it could be reproduced for other applications.

Then we propose several numerical tests. We discuss the results, using images computed by the heuristic for the visual perception, and the associated values of the quantitative criterions. We start by a full example; we observe several reconstructed views; we examinate the surfacic pixels for one view, both visually and quantitatively. In particular it is shown that the *wrong* pixels do not

necessarily disturb the visual perception. The mathematical analysis distinguishes the contributions of smooth data and of discontinuites; we propose to observe separately these contributions. We test the effect of adding jumps, and the effect of increasing the (spatial) frequency of the smooth part. In particular it is shown that the reconstruction has an interest for the visual perception of non-convex objects. The proposed mathematical framework allows changes in the forward model when the angle changes. We show by a test of robustness that this works: we investigate the effect of disturbing more and more the forward model. Concerning the resolution, we realize a test by increasing more and more the size of the dataset; more and more details are captured as wanted. And for the stability, we test the effect of adding more and more speckle noise. The result is that the method is stable; even better, reconstructed views can look better than the original views for large levels of noise. We can also read transversely the numerical tests to make further observations. We have tests for several forward models: binary dataset, Lambert-kind model, Gouraud model, and fluctuating models. We have an example of adjustement of the colormap, and we have also an example of visualization of an extracted sub-domain. All of these numerical tests are original. They confer a very large credibility to the heuristic and the proposed interpretation. In order to drive home the abilities of the method, we show furthermore an example of application, from a set of experimental laser data. In comparison with [19], the renderings are improved.

The paper is organized as follows. In the first part, we define and discuss the computational heuristic of reconstruction and visualization in a mathematical framework. In the second part, we test the relevance of the approach on a wide variety of examples. We finish by an example of application.

2 Computational heuristic for 3D imaging

2.1 Reflective cone beam scanning

We define a mathematical model for the cone beam scanning of a reflective-kind scene.

In the space $\mathbb{R}^3$, we consider that an object is a bounded domain $\Omega \subset \mathbb{R}^3$ with a boundary $\Sigma = \partial\Omega$; a surfacic function $f : \Sigma \to \mathbb{R}$ is called an intensity (or an information) of the object Σ. We consider a set of n separated objects, with boundaries $\Sigma_i, 1 \leqslant i \leqslant n$. We also consider a wall, or background, Σ_0, as a surface whose interior domain contains the whole scene. This convention for the wall allows to treat the background exactly as the objects of the scene. For convenience, $\Sigma = \cup_{0 \leqslant i \leqslant n} \Sigma_i$ is the set of surfacic points; when the f_i are the intensities of the Σ_i, f_Σ is the intensity of Σ: for $v \in \Sigma_i$, $f_\Sigma(v) = f_i(v)$.

Let $\beta \in [0, 2\pi]$ be a fixed angle. We consider a device on the circle $|x| = r > 0$ in the plane $x_3 = 0$, at the position $r\theta = r(\cos\beta, \sin\beta, 0)$. We assume that the device contains a receptor array on which we record a cone beam projection of the scene, along rays through the optical center $r\theta$. The plane $\theta^\perp = \{x \in \mathbb{R}^3 : x \cdot \theta = 0\}$ passes through the origin and is parallel to the receptor array. For the ray $L(\theta, y)$ through $r\theta$ and $y = y_2\theta_\perp + y_3 e_3 \in \theta^\perp$, with $\theta_\perp(\beta) = (\sin\beta, -\cos\beta, 0)$ and $e_3 = (0, 0, 1)$, the visible point of the scene is $v(\theta, y)$, which is the first intersection point of the ray $L(\theta, y)$ with the surfaces Σ_i: $v(\theta, y) = r\theta + \rho(\theta, y)(y - r\theta)$, with $\rho(\theta, y) = \arg\min\{\rho, \rho > 0, v = r\theta + \rho(y - r\theta) \in \Sigma\}$. We consider an information on Σ: $v \in \Sigma \mapsto f_\Sigma(v, \theta)$. The first variable $v \in \Sigma$ represents a surfacic point, whereas the second variable θ indicates that the information depends on the angle θ. On the ray $L(\theta, y)$, we record an information $F_\theta(y)$ coming from the visible point $v(\theta, y)$: $F_\theta(y) = f_\Sigma(v(\theta, y), \theta)$. This process of reflective projection is illustrated on Figure 1. Assuming that (y_2, y_3) scans a rectangle $[-a, a] \times [-b, b]$, the record is a bi-dimensional image $y \mapsto F_\theta(y)$; we call F_θ the reflective projection, associated with the angle θ.

In the Figure 1, we also represent a 2D beam which intersects the screen on a horizontal line $y_3 = C$. It is reasonnable to assume that for such a beam, the resulting horizontal slice in the image F_θ is a piecewice smooth function. More precisely, we denote by E the space of functions $g : [-a, a] \to \mathbb{R}$ that are piecewise $\mathscr{C}^1$ and whose pieces can be extended by continuity: $g \in E$ if, and only if, there exists a (finite) subdivision $-a = s_0 < \cdots < s_j < \cdots < s_{N+1} = a$ and there exists a family of functions $g_j \in \mathscr{C}^1((s_j, s_{j+1})) \cap \mathscr{C}^0([s_j, s_{j+1}]), 0 \leqslant j \leqslant N$, such that $\forall s \notin \{s_j, j\}, g(s) =$

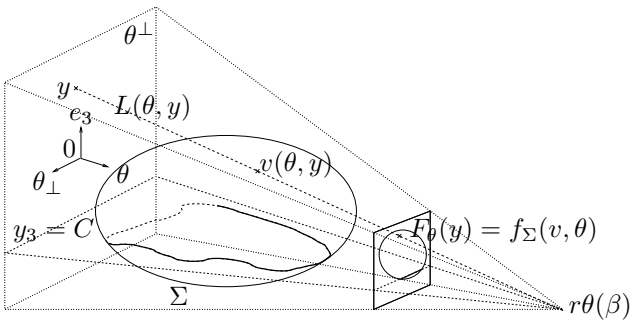

Figure 1: Reflective cone beam projection. The ray $L(\theta, y)$ passes through the optical center $r\theta(\beta)$ and the point $y = y_2\theta_\perp + y_3 e_3 \in \theta^\perp$. The visible point is $v = v(\theta, y) \in \Sigma$, and the record is: $F_\theta(y) = f_\Sigma(v, \theta)$. A horizontal slice in the recorded image is also represented. The intersection of Σ with the 2D beam $y_3 = C$ is represented (without the background); in bold: the visible part of the surface and its projection.

$\sum_{j=0}^{N} g_j(s)\mathbb{1}_{(s_j, s_{j+1})}(s)$. For convenience we extend $g \in E$ by zero: $g(s) = 0$ for $|s| > a$. We assume that for every y_3, the horizontal projection $y_2 \mapsto F_\theta(y)$ belongs to the space E, with the following piecewise smooth decomposition:

$$F_\theta(y) = \sum_{j=0}^{n_{\theta,y_3}} f_\Sigma(v(\theta, y), \theta)\mathbb{1}_{(s(\theta,y_3,j), s(\theta,y_3,j+1))}(y_2). \tag{1}$$

On the piece $(s(\theta, y_3, j), s(\theta, y_3, j+1))$, the visible part of the scene is a subset of the object number $i(\theta, y_3, j)$: $\Sigma(\theta, y_3, j) = \{v(\theta, y), y_2 \in (s(\theta, y_3, j), s(\theta, y_3, j+1))\} \subset \Sigma_{i(\theta,y_3,j)}$. The visible curve $\Sigma(\theta, y_3, j)$ is also a subset of the 2D beam $(r\theta, -a\theta_\perp + y_3 e_3, a\theta_\perp + y_3 e_3)$. The piece $\Sigma(\theta, y_3, j)$ is furthermore assumed to be $\mathscr{C}^1$. The following reasons explain horizontal discontinuities in the image F_θ:

- geometrical jump: the consecutive visible pieces $\Sigma(\theta, y_3, j)$ and $\Sigma(\theta, y_3, j+1)$ are not linked: $v(\theta, y)$ jumps from one object to another object, or jumps from one part of a non-convex object to another part of the same object;
- tangential jump: the pieces $\Sigma(\theta, y_3, j)$ and $\Sigma(\theta, y_3, j+1)$ are included in the same object Σ_i and are linked, so $v(\theta, y)$ is continuous, but the intensity of the object f_i jumps.

(See subsection 3.2 to observe these two kinds of jumps.)

Finally, we change the acquisition angle and we restart: this experiment is repeated for θ scanning a finite set of angles $\Theta \subset \mathrm{S}^1 \times \{0\}$, whose cardinal is $|\Theta|$. Juxtaposing the different images, we get at the end a 3D *reflectogram* $(y, \theta) \mapsto F_\theta(y)$. In the reflectogram, each surfacic point $v \in \Sigma$ is seen partially (or eventually not seen) along the curve $\{(\theta, y) : v \in L(\theta, y)\}$; its intensity level depends on θ. The main challenge is transforming the reflectogram to images that are usable for identification of the surfaces Σ_i.

2.2 Tomography solver

We recall the heuristic of reflective tomography: applying the FDK algorithm on the reflectogram.

The first step is weighting the dataset:

$$F_w(\theta, y) = w(y)F_\theta(y), \text{ with } w(y) = \tfrac{r}{(r^2 + {y_2}^2 + {y_3}^2)^{0.5}}. \tag{2}$$

The next step is computing a tomographic horizontal filtering of the weighted dataset F_w. We recall that a regularized kernel of the Hilbert transform is $\varphi = \mathcal{F}^{-1}(-\mathrm{i}\,\mathrm{sign}(\sigma) \cdot \hat{h}(\sigma))$, where $\mathcal{F}$ is the Fourier transform and $\hat{h}(\sigma)$ is an even windowing function with compact support (σ is the frequency). For $g \in E$, g is a distribution with compact support, so the tomographic filtering $\partial_s g \star \varphi$

of g is defined and satisfies: $\partial_s g \star \varphi = \mathcal{F}^{-1}(|\sigma|\,\hat{h}(\sigma)\mathcal{F}(g)(\sigma))$. For all $y_3 \in [-b,b]$, we define and compute the filtering of $y_2 \mapsto F_w(\theta,y) \in E$:

$$\partial_{y_2} F_w \star \varphi = \mathcal{F}^{-1}(|\sigma|\,\hat{h}(\sigma)\mathcal{F}(F_w(\theta,y))(\sigma)), \tag{3}$$

where the Fourier transform is taken with respect to y_2.

The last step is computing a weighted backprojection f_{FDK}: for each reconstruction point x, we sum over lines through x in the weighted filtered weighted reflectogram:

$$f_{\mathrm{FDK}}(x) = \sum_{\theta\in\Theta} \frac{r^2}{(r - x\cdot\theta)^2}(\partial_{y_2} F_w \star \varphi)(\theta, y), \tag{4}$$
$$\text{with } y = \frac{rx\cdot\theta_\perp}{r-x\cdot\theta}\theta_\perp + \frac{rx_3}{r-x\cdot\theta}e_3.$$

Concerning practical aspects, the reflectogram F is known on a 3D discrete grid of size $|\Theta| \times N_2 \times N_3$. The horizontal filtering $\partial_{y_2} F_w \star \varphi$ is computed on the same grid, using the Fast Fourier Transform; in this paper, we will choose the Shepp-Logan filter: $\hat{h}(\sigma) = \frac{\sin\frac{\pi}{2}\frac{\sigma}{\sigma_{\max}}}{\frac{\pi}{2}\frac{\sigma}{\sigma_{\max}}}\mathbb{1}_{-\sigma_{\max}\leqslant\sigma\leqslant\sigma_{\max}}$, where $\sigma_{\max}$ is the Nyquist frequency. The computational cost for filtering is $\mathcal{O}(|\Theta|\,N_3N_2\log N_2)$. The reconstruction f_{FDK} is computed on a 3D grid of voxels. For N^3 voxels, the cost is $\mathcal{O}\left(N^3\,|\Theta|\right)$; it is known to be the most consuming step. To speed up the computations, strategies of implementation on GPU are available in the literature. Basically, for the last step, each thread can be the computation of the backprojection for one voxel.

2.3 Reflective tomography: analysis and discussion

We give an interpretation of a reflective FDK volume, based on the previous mathematical model.

A key point in the processing is the filtering step: $\partial_{y_2} F_w \star \varphi$. The derivative enhances the horizontal contrasts of the (weighted) reflectogram. Using the jumps formula from the theory of distributions, we get two contributions:

$$\partial_{y_2} F_w = \sum_{j=0}^{n_{\theta,y_3}} \partial_{y_2} w(y) f_{i(\theta,y_3,j)}(v(\theta,y),\theta)\mathbb{1}_{(s(\theta,j),s(\theta,j+1))} + \sum_{j=0}^{n_{\theta,y_3}+1} w(s(\theta,y_3,j))[f_{\theta,y_3,j}]\delta_{s(\theta,y_3,j)},$$

where the $[f_{\theta,y_3,j}]$ are the jumps accross the discontinuities of $y_2 \mapsto F_\theta(y)$; after the filtering: $\partial_{y_2} F_w \star \varphi = C_{\mathrm{S}} + C_{\mathrm{J}}$, where

$$C_{\mathrm{S}} = \sum_{j=0}^{n_{\theta,y_3}} \int_{s(\theta,y_3,j)}^{s(\theta,y_3,j+1)} \partial_{y_2} w(y) f_\Sigma(v(\theta,y),\theta)|_{y_2=y_2'}\,\varphi(y_2-y_2')\mathrm{d}y_2', \tag{5}$$

$$C_{\mathrm{J}} = \sum_{j=0}^{n_{\theta,y_3}+1} w(s(\theta,y_3,j))[f_{\theta,y_3,j}]\varphi(y_2 - s(\theta,y_3,j)). \tag{6}$$

The term C_{S} is due to the smooth variations of the (weighted) intensities f, along curves of visible surfacic points. The term C_{J} is due to the horizontal jumps of intensities in the record. The contribution of these terms will be illustrated in subsections 3.3 and 3.2. In practice the kernel φ becomes rapidly small; thus the filtering detects the contours that are transverse to the horizontal direction in the dataset. The kernel φ is odd, so it is a detection of zero-crossing type.

The (weighted) backprojection recombines finally all the contrasts in space. We can now discuss the effect of this summation. For a generical reconstruction point x, the filtered informations through x are *incoherent*; they tend to compensate for each other by summation. But, when x is near a surfacic point v which is visible under some angular range, the associated filtered data can contain a *coherent* part which produces a significant value at x by summation. This discussion motivates the following interpretation: "the reflective tomography recombines the coherent horizontal contrasts at their true location in space".

2.4 Efficient visualization

We describe an efficient way of visualizing a volume in reflective tomography.

The heuristic computes a 3D volume that needs to be correctly investigated to recognize the objects of the original scene. In order to appreciate 3D structures, surface rendering or volume rendering are better than slicing. Surface rendering produces surfaces of the scene; unfortunately it needs hard thresholding and it may produce lacunarities. Here we prefer volume rendering; it produces automatically images of the scene, from the full volume. Basically, volume rendering is simulating a scanner: to display a function $f : \mathbb{R}^3 \to \mathbb{R}$, it computes and displays a projection $P[f]$ on a 2D screen: see Figure 2. We can get several kinds of visualization, depending on the choice of the projection operator. The projection looks often like a $\mathscr{L}^p$-norm over the ray: forall ray L, the projection along the ray L is: $P[f](L) = \| f|_L \|$. Among these methods, the X-Ray visualization is the X-Ray transform $P[f](L) = \int_L f$, and the Maximum Intensity Projection (MIP) is $P[f](L) = \max_L(f)$.

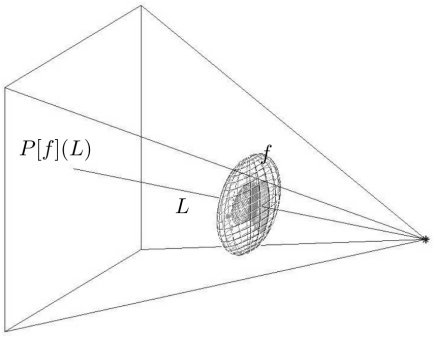

Figure 2: Principle of volume rendering: to display a volumetric function $f : \mathbb{R}^3 \to \mathbb{R}$, we display a 2D projection $P[f]$ on a screen.

How to display the reconstruction f_{FDK} ? We expect that surfaces of the scene produce significant values in f_{FDK}, whereas we expect low values at voxels far from the surfaces. As a result, if we want to display the surfaces, we need to select the significant values in f_{FDK} and to eliminate the others. This job will be very well performed by MIP: by definition, along each ray of projection, it selects and displays only the most intense voxel. Thus MIP[1] of f_{FDK} tries to visualize surfacic points of the original scene, with a significant value. Also, for the rays which do not intersect the original surfaces, we expect a low value. By the way the MIP is expected to be more than just a visualizing process: due to the selection of only one voxel per ray (and which is probably surfacic), visualizing the volume f_{FDK} by MIP should contain implicitly a processing step which reduces the artifacts and should select the surfaces with the best possible resolution.

We describe now how using the MIP as the visual field of a virtual observer. We consider an observer, whose optical center is located at $x_0 \in \mathbb{R}^3$; we consider that he looks at a point $x_1 \neq x_0$. We consider an orthonormal basis $(\omega_1, \omega_2, \omega_3)$ such that $\omega_1 = \frac{x_1 - x_0}{|x_1 - x_0|}$ and $\omega_3 = \omega_1 \wedge \omega_2$; we assume that the rays of the visual field are the $x_0 + \rho(\omega_1 + y_2\omega_2 + y_3\omega_3)$, $|y_2| < Y_2$, $|y_3| < Y_3$, $0 < \rho$. We assume that the part of the scene to be visualized is a domain Ω; Ω is the whole volume by default. We can define the view V as the set of these parameters: $V = (x_0, x_1, \omega_2, Y_2, Y_3, \Omega)$. We simulate the visual field of the observer by computing, for $|y_2| < Y_2, |y_3| < Y_3$:

$$J_V(y_2, y_3) = \max\{f_{\text{FDK}}(x), x = x_0 + \rho(\omega_1 + y_2\omega_2 + y_3\omega_3) \in \Omega, \rho > 0\}. \tag{7}$$

To get the representation of $y_2 \in [-Y_2, Y_2] \times [-Y_3, Y_3] \mapsto J_V(y_2, y_3)$, we set a RGB colormap $\Gamma : \text{Range}(J_V) \to [0, 255]^3$, and we display the image:

$$I_V = \Gamma[J_V]. \tag{8}$$

[1]By choosing MIP of f_{FDK}, we implicitely decide to focus on the non-negative values of f_{FDK}. It could also be possible to focus on the most intense negative values, by considering the Minimum Intensity Projection, or to keep all the values by considering $|f_{\text{FDK}}|$ instead of f_{FDK}.

We would like to emphasize in the rendering the non-negative intense values of f_{FDK}, so we impose the following conditions: $\Gamma(t) = 0$ for $t < 0$ and $\|\Gamma(t)\|$ is a non-decreasing function. This colormap Γ can eventually improve the rendering by including rescalings or thresholdings. In this paper, we produce grayscale images by assuming that the three RGB channels are the same: $\Gamma(t) \in [0, 255]$, and to fix ideas, we make the following choice by default: once J_V is computed, we set

$$\Gamma(t) = \begin{cases} 0, & t \leqslant 0, \\ \frac{255}{T} t, & 0 \leqslant t \leqslant T, \\ 255, & T \leqslant t, \end{cases} \quad \text{where } T = 0.5 \max J_V. \tag{9}$$

With such a choice, $I_V = \Gamma[J_V]$ is a thresholded version of J_V, whose range is $[0, 255]$ due to the linear scaling.

Concerning implementation aspects, an image $I_V(y_2, y_3)$ is computed on a discrete grid of size $n_2 \times n_3$, from a discrete volume. One pixel corresponds to the projection along one ray. This may require interpolation. When the size of f_{FDK} is N^3 and Ω is the full volume, the cost for I_V is $\mathcal{O}(n_2 n_3 N)$. To speed up the computations, it is possible to implement the MIP on GPU. For example, each thread can be the computation of one pixel of the image I_V.

In practice, a view V and a colormap Γ can be decided in advance; in that case, the image I_V is computed completely automatically. Then several views can be computed by changing the parameters: the optical center x_0 can be translated, the central point x_1 can be translated, the directions of the image ω_2, ω_3 can be rotated, the apertures Y_2 and Y_3 can be changed to zoom in/out, and the extracted sub-volume Ω can be changed. Adjusting the colormap Γ adjusts the rendering. Whereas changing the view V can be a way to obtain displacements in the scene, or videos, which helps to appreciate 3D structures.

2.5 Summary: global process

Combining the heuristic of reconstruction and the visualization principle, we get a computational process that can generate new views of a reflective scene: see Table 1. The reconstruction (step 1) is computed once for all; to change the view, we change V and we apply only the projection (step 2).

Input: reflectogram F, parameters of the view V
Step 1: compute the heuristical reconstruction f_{FDK}, by (2), (3), (4) Step 2: display the image I_V, by projecting f_{FDK} for the view V, by (7) and (8)
Output: image I_V of the reconstructed scene, for the desired view V

Table 1: Global process: a new image I_V of the scene is displayed for the desired view V, from the reflectogram F.

We represent a reflective cone-beam scanning as $F = \Pi f_\Sigma$. For each angle θ, the scene is represented by a distribution $f_\Sigma(v, \theta)$ supported by the surface Σ of the scene; Π is the reflective projection of these distributions. The heuristical solver computes the FDK reconstruction $f_{\mathrm{FDK}} = \mathcal{R}^* \Phi F$ from the reflectogram F; the operation Φ realizes (2) and (3), whereas $\mathcal{R}^*$ is the weighted backprojection (4). For a desired view V, the visualization step computes the MIP $J_V = P_V f_{\mathrm{FDK}}$ from (7), and the result is displayed with the colormap Γ: $I_V = \Gamma J_V$. In a word, the global heuristic generates the image I_V from the reflectogram Πf_Σ by:

$$I_V = \underbrace{\Gamma \, \underbrace{P_V \, \underbrace{\mathcal{R}^* \, \underbrace{\Phi \, \underbrace{\Pi f_\Sigma}_{F}}_{f_{\mathrm{FDK}}}}_{J_V}}}.$$

2.6 Quality control

The quality control of results for synthetic tests will be based on the visual perception (main criterion), and on quantitative criterions.

How to define such quantitative criterions? This question is more difficult than it appears. A (bad) idea could be controlling the quality of the heuristical reconstruction f_{FDK}, by comparing it with f_Σ. First this is not possible because f_{FDK} and f_Σ are different mathematical objects: f_Σ is a set of surfacic distributions which depend on the angle (the $f_i(v,\theta)$) whereas f_{FDK} is a fixed volumetric function. Secondly f_{FDK} is just a heuristic representation of the scene; so even on Σ, we can imagine that f_{FDK} is different from the $f_i(v,\theta)$. This is a big difference with transmission tomography where f_{FDK} must be close to a (fixed) volumetric function of attenuation. So we cannot directly define an error between f_{FDK} and f_Σ.

We propose to control the quality of the full process, by checking that an image $I = I_V$ is a right representation of the surface Σ: the main goal is to check that the final image is nice. Fundamentally we would like to check that the significant values of the image I come from voxels which are close to the surfaces of the original scene. If this is indeed the case, then it confirms two things: the most intense values of the heuristical reconstruction are located near the original surfaces, and the produced image represents an image of the surfaces. Otherwise the reconstruction contains high values, which are far from the surfaces and which introduce wrong alarms in the visualization: the final image contains wrong significant informations; they may escape visual perception, or not. We propose criterions which are based on counting the pixels in I that correspond to surfacic voxels.

For a pixel (y_2, y_3) of the image I, the displayed intensity is $I(y_2,y_3) = \Gamma f_{\text{FDK}}(x(y_2,y_3))$, where the voxel $x(y_2,y_3)$ is an $\arg\max$ in (7). The distance between this voxel and the surfaces of the scene is $d(y_2,y_3) = \min\{|x(y_2,y_3) - z|\,, z \in \Sigma\}$. Assuming that a voxel is a cube of volume δ^3, we claim that the voxel $x(y_2,y_3)$ coincides with a surfacic point when $d(y_2,y_3) < \delta$; in that case, we say that $x(y_2,y_3)$ is a *right voxel*, and that (y_2,y_3) is a *surfacic pixel*. (Eventually we could choose another threshold t for the test of being a right voxel: $d(y_2,y_3) < t$ instead of $d(y_2,y_3) < \delta$).

Let N be the number of surfacic pixels in I: $N = \sum_{(y_2,y_3)} \mathbb{1}_{d(y_2,y_3)<\delta}$; the proportion of surfacic pixels in I is $\mu = N/(n_2 n_3) \in [0,1]$. N and μ depend on the geometry of the scene and on the selected view V. The higher μ is, the higher the surfaces are spreaded in I. We can also compute the proportion of intensity explained by the surfacic pixels in I:

$$p = \frac{\sum_{(y_2,y_3)} I(y_2,y_3)\mathbb{1}_{d(y_2,y_3)<\delta}}{\sum_{(y_2,y_3)} I(y_2,y_3)} \in [0,1].$$

We would like p to be the large: the higher p is, the more the intensity in I comes from right voxels. The average of the (normalized) intensity among the surfacic pixels is $\frac{p}{N}$. The ratio $\kappa = \frac{p}{\mu}$ represents a normalized concentration of the intensity among the surfacic pixels. We would like this concentration κ to be large.

The analogous quantities can be defined for the non-surfacic pixels (pixels (y_2,y_3) such that $d(y_2,y_3) \geqslant \delta$): proportion $1-\mu$ for the number, proportion $1-p$ for the intensity, and $\bar{\kappa} = \frac{1-p}{1-\mu}$ for the concentration; we would like $\bar{\kappa}$ to be small. The ratio of the concentrations $\frac{\kappa}{\bar{\kappa}}$ gives an information on how much the surfacic pixels are intense, comparing with the non-surfacic ones; we would like this ratio to be large.

3 Numerical results

3.1 Example

We illustrate the process on a full example.

3.1.1 Reflectogram

We simulate a reflectogram, from the famous Stanford Bunny [23]. We use the full resolution dataset: 69451 faces. We use the lighting functionnalities of Matlab. For that example, we color

the faces of the object, using the following smooth pattern:

$$x \mapsto 1 + 0.5 \sin(20\pi\,|x|);$$

the pattern is computed at the vertices, and extended to the faces by interpolation. We consider a black background: intensity $f_0 = 0$. We use the Gouraud model of Matlab for the lighting model. The object is rotated over 360 degrees (constant step); we take $|\Theta| = 1605$ images of size $N_2 \times N_3 = 397 \times 312$. We represent 6 images of this sequence in the Figure 3.

3.1.2 Heuristic

We apply the process of reconstruction-visualization. For the filtering, we choose the Shepp-Logan filter. We compute two sequences of displacements around the reconstructed scene: for the first one, we turn around the vertical axis, for the second one, we turn around a horizontal direction: see Figure 4 for the resulting images. The visual perception of the results is nice. The renderings are contrasted. They represent the original scene under a semi-transparent form. The different surfaces are somehow mixed together; in particular, views from opposite sides look similar. A way of improving the visual perception is creating videos where the view changes continuously, and/or reducing the displayed volume Ω.

3.1.3 Quality control

We now control the quality of the rendering by controlling a set of surfacic pixels. We must select one view. The focal planes of the acquisition are vertical, so generating a view on a horizontal plane is morally one of the most difficult problems. That is the reason why we decide here to select an aerial view: we control the process of generating a semi-transparent aerial view from vertical reflective projections.

To check if a pixel (y_2, y_3) of the rendering is a surfacic pixel or not, we need to estimate the distance $d(y_2, y_3)$ of the voxel $x(y_2, y_3)$ and the surfaces of the scene. Here the scene is the bunny over a black wall. So $d(y_2, y_3)$ is the distance between the bunny and $x(y_2, y_3)$. First we compute a refinement of the bunny: forall face, we compute the vertices of a lattice such that each edge length of the lattice is at most the edge length δ of a voxel. At the end we get a finite set B of vertices. We consider that B is a discrete representation of the bunny for the resolution δ. Then forall pixel (y_2, y_3) of the image I, we estimate the distance between the associated voxel $x(y_2, y_3)$ and the bunny as

$$d(y_2, y_3) = \min\{|x(y_2, y_3) - w|\,, w \in B\}.$$

After the computation of d, we decompose here I into two components; I is the superposition of: I restricted to the detected surfacic pixels $(y_2, y_3) \mapsto I(y_2, y_3)\mathbb{1}_{d(y_2,y_3)<\delta}$, and I restricted to the non-surfacic pixels $(y_2, y_3) \mapsto I(y_2, y_3)\mathbb{1}_{d(y_2,y_3)\geqslant\delta}$. In order to appreciate visually this decomposition we represent I and its components in the Figure 5. The component of the surfacic pixels is sharper than the total image I. But the contribution of the non-surfacic pixels helps for the perception of the object in I.

For the quantitative criterions, we obtain the following values:

N	μ	p	κ	$\bar{\kappa}$	$\frac{\kappa}{\bar{\kappa}}$
23558	0.15	0.43	2.91	0.66	4.38

And so $\mu = 15\%$ of the pixels in the image I come from right voxels; they explain $p = 43\%$ of the total intensity of I. So the concentration of intensity for the surfacic pixels is quite strong: $\kappa = 2.91$. This is $\frac{\kappa}{\bar{\kappa}} = 4.38$ times the concentration for the non-surfacic pixels: $\bar{\kappa} = 0.66$.

3.2 Contribution of the jumps

To observe the contribution of the jumps (see (6)), we create synthetic datasets whose images are piecewise constant. We increase the number of jumps from a dataset to the next one.

We consider here a sphere with a dent. To create this object, we deform the sphere $|x| = 1$, in spherical coordinates (ψ, φ, ρ), where $\psi \in [-\pi, \pi]$ is the azimuth, $\varphi \in [-\frac{\pi}{2}, \frac{\pi}{2}]$ is the elevation, and $\rho > 0$ is the radius. Forall point of the sphere $(\psi, \varphi, \rho = 1)$, the point of the considered surface is $(\psi, \varphi, \rho := 1+0.75(r-1)\mathbb{1}_{r<1})$, with $0.08r := (\frac{\psi}{\pi}+1/4)^2+(\frac{2\varphi}{\pi}+1/6)^2$. This object is computed from a discrete version of the sphere, discretized with 640^2 patches. For all integer m, we define on this surface the following piecewise constant pattern, in spherical coordinates: $(\psi, \varphi) \mapsto p_m(\psi)p_m(\varphi)$, with:

$$p_m(s) = 0.5 + 0.25\mathbb{1}_{(ms-\lfloor ms \rfloor)<0.5}.$$

We project directly this pattern: for a point $v(\psi, \varphi, \rho)$ which is visible for the angle of projection θ, the information which is measured on the corresponding ray is $f(v, \theta) = p_m(\psi)p_m(\varphi)$. And we consider a black background. Such a reflectogram is simulated using plots of surfaces with Matlab. By rotating over 360 degrees, we simulate here datasets whose size is $|\Theta| \times N_2 \times N_3 = 801 \times 201 \times 201$.

Increasing m increases the number of jumps; we simulate datasets for several values of m: 0, 1, 2, 4, 8 and 16. On the first line of Figure 6, we represent one image of the reflectogram, for the successive values of m. Of course we distinguish two kinds of jumps in the images: jumps due to discontinuities in the pattern (tangential jumps), and jumps due to the shape: interface object/background (geometrical jumps).

We apply the heuristic on these datasets. In order to improve the visual perception of the dent, we restrict the domain to a half-space Ω before visualization: our full volume being a set of voxels $(i, j, k) \in [1, 201]^3$, we keep only the $j \geqslant 91$. On the second line of Figure 6, we represent a vertical view of the reconstructions, associated to the view of the datasets. More jumps in the input reflectogram can improve the visual perception of the object, for both the input and the output. The heuristic computes much more than just a convex hull. A remarkable property here is that the dent is even more perceptible in the reconstruction than in the reflectogram. This is because the boundary $(\frac{\psi}{\pi} + 1/4)^2 + (\frac{2\varphi}{\pi} + 1/6)^2 = 0.08$ of the dent introduces geometrical jumps in many input images; the heuristic recombines them, and so the boundary is emphasized in the reconstruction.

To compute the quantitative appreciations, we first compute the distances $d(y_2, y_3)$ from the voxels $x(y_2, y_3)$ to the vertices of the surface, discretized with 640^2 patches. The following table summarizes the results:

m	0	1	2	4	8	16
N	19844	20015	19676	18747	17440	18744
μ	0.49	0.50	0.49	0.46	0.43	0.46
p	0.68	0.69	0.69	0.70	0.70	0.71
κ	1.38	1.38	1.42	1.51	1.63	1.54
$\frac{\kappa}{\bar{\kappa}}$	2.17	2.22	2.34	2.72	3.13	2.87

It is difficult to observe significative rules from these values. We can anyway make the following comments. If we compare the first three cases with the last three cases: the proportion μ of surfacic pixels decays, their proportion p of intensity increases, and so do their concentration κ and the ratio of concentrations $\frac{\kappa}{\bar{\kappa}}$. In a word, adding jumps on the surface changes the visual perception of the scene, and it gives more weight to the surfacic pixels in the rendering.

3.3 Contribution of the smooth variations

Realistic images of realistic scenes have often jumps and variations. Here we would like to observe the contribution (5) of the variations. So we create synthetic datasets whose images are smooth, and whose *frequency* increases from a dataset to the next one.

We consider the sphere $|x| = 1$, which is discretized using 640^2 patches as before. We consider a black background, and we project a smooth pattern, in spherical coordinates:

$$(\psi, \varphi) \mapsto 1 + 0.5 \cos m(\psi + \varphi),$$

with $m = 2^i, 1 \leqslant i \leqslant 6$, playing the role of a fixed frequency. By rotating over 360 degrees, we simulate here reflectograms whose size is $|\Theta| \times N_2 \times N_3 = 801 \times 201 \times 201$. The simulated images are smooth, except at the interface object/background where discontinuities occur. So we weight the data in order to obtain smooth images. For a pixel $(i, j) \in [1, 201] \times [1, 201]$, the weight is $(r+1)^2(r-1)^2 \mathbb{1}_{r<1}$, with $99r(i, j) = ((i-100)^2 + (j-100)^2)^{0.5}$. On the first line of Figure 7, we represent one smooth image of the reflectograms that we get, for the successive values of m.

We apply the heuristic on these datasets. On the second line of Figure 7, we represent a vertical view of the reconstructions, associated to the view of the datasets. And we summarize in the following Table the quantitative criterions that we get for these views:

m	2	4	8	16	32	64
N	1930	1761	1273	3881	10425	17341
μ	0.05	0.04	0.03	0.10	0.26	0.43
p	0.02	0.03	0.02	0.09	0.28	0.54
κ	0.40	0.59	0.73	0.95	1.10	1.26
$\frac{\kappa}{\bar{\kappa}}$	0.39	0.58	0.72	0.95	1.14	1.56

From the visual point of view, it is easier to identify the original sphere for large m. Increasing m also improves the result from a quantitative point of view; all the computed criterions tend indeed to increase: the proportion μ of surfacic pixels, their proportion p of intensity, their concentration κ, and the ratio of concentrations $\frac{\kappa}{\bar{\kappa}}$. For smooth data, the result of the heuristic may be poor for low frequencies components, but is meaningful when the frequency is large enough. In any case, the smooth variations of the input produce contrasts in the renderings; they can be useful for the visual perception.

3.4 Test of robustness

We show how the method deals with changes in the forward problem during the acquisition, by considering a randomized fluctuating model.

For all $\sigma = 0, 2^j, -2 \leqslant j \leqslant 2$, we consider a scan $F_\sigma(\theta, y_2, y_3)$ over 360 degrees of the Stanford Bunny; the size of this scan is $|\Theta| \times N_2 \times N_3 = 801 \times 200 \times 157$. For each angle θ, the projected surfacic pattern (with background $f_0 = 0$) is:

$$x \mapsto 1 + (0.2 + \sigma\eta_1(\theta)) \sin(\pi\sigma\eta_2(\theta) + 20\pi\,|x|),$$

where the $\eta_i(\theta)$ are independant realisations of the gaussian $\mathcal{N}(0, 1)$. The $\sigma\eta_i(\theta)$ correspond to some modifications of the amplitude and the phase of the pattern. Increasing σ increases the dependancy in θ for the projected pattern. Along a piece of curve $\{(\theta, y) : v \in L(\theta, y)\}$ where v is a visible point of the scene, the intensity level of v randomly varies with a standard deviation which increases when σ increases. To observe this, see the first line of Figure 8, where we represent the horizontal slice $y_3 = 0$ of the considered reflectograms.

We apply the heuristic on these datasets. On the second line of Figure 8, we represent a vertical view of the reconstructions; we get the following quantitative appreciations:

σ	0.00	0.25	0.50	1.00	2.00	4.00
N	11805	11644	11410	11373	10745	8456
μ	0.38	0.37	0.36	0.36	0.34	0.27
p	0.79	0.77	0.74	0.69	0.61	0.42
κ	2.11	2.09	2.03	1.92	1.78	1.57
$\frac{\kappa}{\bar{\kappa}}$	6.36	5.82	4.94	4.00	2.99	2.00

Despite changes in the forward problem, some informations stay coherent. This is for example the case of the shape of the object. The visual perceptions that we get here tend to show that the heuristic successfully recombines such coherent informations, which is in agreement with the discussion of subsection 2.3. From a quantitative point of view, the computed criterions decay slowly when the level of disturbance increases. Increasing the disturbance does not seriously affect the set of right voxels in the final image, from the cardinal point of view, and from the intensity point of view too. It is also clear that the result stays relevant for large disturbances; for the last case, despite the level of disturbance is about 4 times the intensity level of the original signal, surfacic variations can still be percepted in the reconstruction.

3.5 Test of resolution

We oberve the effect of increasing the resolution of the reflectogram on the reconstructed images.

The set-up is exactly as in the subsection 3.1, except that we consider several sizes of datasets. For an image whose horizontal length is $N_2 = \ell + 1$ pixels, we choose $|\Theta| = \lceil \ell\pi \rceil$ angles, over $[0, 2\pi)$. We choose such a sampling because it is compatible with sampling conditions of transmission tomography. On the first line of Figure 9 we represent one image of each reflectogram.

On the second line we represent an associated heuristical reconstruction, with the colormap (9). We propose here a second choice of colormap: in (9), we replace the upper threshold by the quantile of $\max(J_V, 0)$ for the cumulative probability 97%: $T_2 = \text{quantile}(\max(J_V, 0), 0.97)$. We get a colormap which is based on the cumulative histogram; the result is less sensitive to the single value $\max(J_V, 0)$ of the histogram. This avoids the apparent loss of contrast when the resolution increases: see the third line of Figure 9. From the visual point of view, increasing the resolution of the dataset improves the sharpness of the reconstruction. The global shape is sharper and sharper; more and more details are perceptible to the eye: see for example the coat.

The values for quality control are (for the threshold T_2):

$\lvert\Theta\rvert$	48	98	198	399	802	1204
N_2	16	32	64	128	256	384
N_3	14	26	52	102	202	302
N	113	360	1219	4308	15263	32141
μ	0.50	0.43	0.37	0.33	0.30	0.28
p	0.81	0.81	0.74	0.70	0.65	0.63
κ	1.61	1.87	2.02	2.13	2.21	2.28
$\frac{\kappa}{\bar{\kappa}}$	4.20	5.63	4.93	4.77	4.51	4.46

Some parameters slowly decrease when the resolution increases: the proportion μ of surfacic pixels, their proportion p of intensity, and the ratio of the concentrations $\frac{\kappa}{\bar{\kappa}}$. From a more optimistic point of view, the number N of right pixels increases, and so does their concentration κ.

3.6 Test of stability

We realize a stability test by adding a speckle noise, for several orders of magnitude of noise.

We consider a reflectogram F as in the subsection 3.5, with a size of $|\Theta| \times N_2 \times N_3 = 801 \times 200 \times 157$; we apply the linear scaling such that the range of F becomes $[1, 2]$: $F := 1 + (F - \min F)/(\max F - \min F)$. For $\sigma = 0.05i, 0 \leqslant i \leqslant 30$, we consider a reflectogram F_σ with a speckle noise of magnitude σ: $F_\sigma = F(1 + \sigma\eta)$, where η contains $|\Theta| \times N_2 \times N_3$ (independant) realizations of the gaussian $\mathcal{N}(0, 1)$.

In the Figure 10 we represent one image of the noisy datasets F_σ, for $\sigma = 0.3i, 0 \leqslant i \leqslant 5$, and we represent the associated reconstructions. We give in the following table the associated quantitative criterions. And in the Figure 11, we plot the criterions as functions of the level of noise, from the

values $\sigma = 0.05i, 0 \leqslant i \leqslant 30$.

σ	0.00	0.30	0.60	0.90	1.20	1.50
N	8252	4033	2459	1838	1576	1400
μ	0.26	0.13	0.08	0.06	0.05	0.04
p	0.59	0.19	0.10	0.07	0.06	0.05
κ	2.23	1.45	1.24	1.17	1.13	1.08
$\frac{\kappa}{\bar{\kappa}}$	3.97	1.56	1.27	1.18	1.14	1.09

Except for the ratio of the concentrations which fastly decays at the very beginning, the criterions slowly decay when the level of noise increases. The visual perception of the reconstructed scene is stable. For large levels of noise, the scene is even better percepted in the reconstruction than in the reflectogram. This is due to the accumulation of coherent informations over the whole dataset.

3.7 Transverse reading

Further observations can be made by reading transversely the previous results.

The method works for several kinds of physical models. In the first example of subsection 3.2, the model is binary; it illustrates the reconstruction of a non-convex object from its shapes. And all of the examples of this subsection are based on projecting a fixed distribution. For the subsections 3.1, 3.5 and 3.6, it is a Gouraud model. In particular, these results include cases of isotropic diffusion without specular components, and cases with both diffusion and specular reflections. And we have even results for fluctuating models in 3.4.

Concerning the rendering, we have semi-transparent representations of full reconstructed volumes, and we illustrate in 3.2 the improvement produced by selecting a sub-domain, which is also a simple way of observing a region of interest. We have by the way proposed renderings based on two thresholding rules. This illustrates the influence of thresholding, and more generally the adjustement of the rendering by changing the colormap.

4 3D optronic imaging

In this section we provide an example of using heuristical cone beam computed optics. We consider a real laser system which provides active laser images of backscattered intensity by rough surfaces: see [19] for technical details of such a device. We consider a set of real optronic images, courtesy of Thales Optronique SA, obtained with this system. A sequence of 360 images of size 342×181 was measured by turning around the scene, one degree step. The considered scene is a vehicle: see Figure 12 for samples of the sequence.

We apply the heuristic, using a home-made software, implemented in CUDA C. The execution on a Nvidia Tesla C2075 takes 2.6 seconds for the reconstruction, and is real-time for the display. In the Figure 13, we represent snapshots that we got interactively. For the first three views, the rendering uses extracted sub-volumes. The next images use the whole volume, with a view clearly different from the recorded views. In particular the last view is taken inside the vehicle. The reconstructed scene contains features and details that are useful for recognition. A notion of relief can be percepted in the rendering. By the way the scene was not completely opaque: transmission accross glasses. The dashboard, which is behind the glasses, is reconstructed. The heuristic and its interpretation of recombination of coherent contrasts still apply for data which are not purely reflective; this extends its domain of validity.

5 Conclusion

This paper deals with a new heuristic designed to compute and display new views of a 3D scene, from a set of cone beam reflective projections. We have proposed a new mathematical framework

for this subject, and an interpretation of the process. The strong potential of the approach is shown on many numerical results, including a real case. As a result we have a high-performance heuristic which answers to the main problem of interest. It is a direct method, suited for massively parallel computing, which enables interactions with the display of the 3D reconstructed scene. The method is for instance applicable in phaseless imaging, from cone beam optical data.

We appreciated the visual aspects of the results. We also proposed new criterions to appreciate them more quantitatively, for synthetic tests. We obtained that the produced images are not rendering illusions: they really contain surfacic points of the initial scene. At the same time, this is an original validation of reflective tomography.

This paper interprets reflective tomography as a combination of the coherent horizontal contrasts at their true location in space, yielding a volume which is essentially supported by the surfaces of the initial scene. This is a way of understanding reflective tomography, which becomes a far-reaching method: possible scenario of use include passive/active, monostatic/multistatic, or monofrequency/multifrequency imagery.

The numerical results have also interests for the applications. We deduce from the tests of stability that the method is interesting for reconstructions from noisy images. The tests of robustness show that the method can be efficient to reconstruct objects with active surfaces emitting countermeasurements. The tests of resolution are a first step toward a proof that high-resolution reconstructions are possible from high-resolution acquisition devices. In a word, there is a real hope of real-time high-resolution 3D reconstructions in optics, even when occlusions, noise and countermeasurements disrupt the acquisition.

References

[1] J.-B. Bellet, I. Berechet, S. Berechet, G. Berginc, and G. Rigaud. Laser Interactive 3D Computer Graphics. *2nd International Conference on Tomography of Materials and Structures, Québec*, 2015. <hal-01175855>.

[2] J.-B. Bellet and G. Berginc. Reflective filtered backprojection. *Submitted*, 2015. <hal-01202974>.

[3] I. Berechet and G. Berginc. Advanced algorithms for identifying targets from a three-dimensional reconstruction of sparse 3D Ladar data. In G. Berginc, editor, *Optical Complex Systems: OCS11, 81720Z*, volume 8172 of *Proc. of SPIE*, 2011.

[4] I. Berechet, G. Berginc, and S. Berechet. Method for 3D reconstruction of an object in a scene. United States Patent, No US 2013/0100131 A1, April 2013.

[5] S. Berechet, G. Berginc, J.-B. Bellet, and I. Berechet. Procédé de discrimination et d'identification par imagerie 3D d'objets d'une scène. Demande de brevet, 2014.

[6] G. Berginc. Scattering models for range profiling and 2D-3D laser imagery. In L. M. Hanssen, editor, *Reflection, Scattering, and Diffraction from Surfaces IV, 92050K*, volume 9205 of *Proc. of SPIE*, 2014.

[7] G. Berginc and M. Jouffroy. Optronic system and method dedicated to identification for formulating three-dimensional images. US patent 20110254924 A1, European patent 2333481 A1, FR 09 05720 B1, November 2009.

[8] G. Berginc and M. Jouffroy. Simulation of 3D laser systems. In *Geoscience and Remote Sensing Symposium, 2009 IEEE International, IGARSS 2009*, volume 2, pages 440–444. IEEE, 2009.

[9] G. Berginc and M. Jouffroy. Simulation of 3D laser imaging. *PIERS Online*, 6(5):415–419, 2010.

[10] G. Berginc and M. Jouffroy. 3D laser imaging. *PIERS Online*, 7(5):411–415, 2011.

[11] J. W. Choe, A. Nikoozadeh, O. Oralkan, and B. T. Khuri-Yakub. GPU-based real-time volumetric ultrasound image reconstruction for a ring array. *Medical Imaging, IEEE Transactions on*, 32(7):1258–1264, 2013.

[12] L. Feldkamp, L. Davis, and J. Kress. Practical cone-beam algorithm. *JOSA A*, 1(6):612–619, 1984.

[13] N. Gac, S. Mancini, M. Desvignes, and D. Houzet. High speed 3D tomography on CPU, GPU, and FPGA. *EURASIP Journal on Embedded systems*, 2008:1–12, 2008.

[14] J. F. Gruden, S. Ouanounou, S. Tigges, S. D. Norris, and T. S. Klausner. Incremental benefit of maximum-intensity-projection images on observer detection of small pulmonary nodules revealed by multidetector CT. *American Journal of Roentgenology*, 179(1):149–157, 2002.

[15] F. Knight, S. Kulkarni, R. Marino, and J. Parker. Tomographic Techniques Applied to Laser Radar Reflective Measurements. *Lincoln Laboratory Journal*, 2(2):143–160, 1989.

[16] S. Napel, M. P. Marks, G. D. Rubin, M. D. Dake, C. H. McDonnell, S. M. Song, D. R. Enzmann, and R. Jeffrey Jr. CT angiography with spiral CT and maximum intensity projection. *Radiology*, 185(2):607–610, 1992.

[17] F. Natterer and F. Wübbeling. *Mathematical methods in image reconstruction*. SIAM, 2001.

[18] D. Riabkov, X. Xue, D. Tubbs, and A. Cheryauka. Accelerated cone-beam backprojection using GPU-CPU hardware. In *9th International Meeting on Fully Three-Dimensional Image Reconstruction in Radiology and Nuclear Medicine*, pages 68–71. Citeseer, 2007.

[19] G. Rigaud, J.-B. Bellet, , G. Berginc, I. Berechet, and S. Berechet. Reflective Imaging Solved by the Radon Transform. *IEEE Geoscience and Remote Sensing Letters*, pages 1–3, to appear.

[20] J. B. Roerdink. Morphological pyramids in multiresolution MIP rendering of large volume data: Survey and new results. *Journal of Mathematical Imaging and Vision*, 22(2-3):143–157, 2005.

[21] H. Scherl, B. Keck, M. Kowarschik, and J. Hornegger. Fast GPU-based CT reconstruction using the common unified device architecture (CUDA). In *Nuclear Science Symposium Conference Record, 2007. NSS'07. IEEE*, volume 6, pages 4464–4466. IEEE, 2007.

[22] A. Sima. Performances study of tomographic reconstruction implented on nvidia graphic processor systems. *University Politehnica of Bucharest Scientific Bulletin, Series C: Electrical Engineering*, 73(2):205–220, 2011.

[23] G. Turk and M. Levoy. Zippered polygon meshes from range images. In *Proceedings of the 21st annual conference on Computer graphics and interactive techniques*, pages 311–318. ACM, 1994.

[24] R. W. Underberg, F. J. Lagerwaard, B. J. Slotman, J. P. Cuijpers, and S. Senan. Use of maximum intensity projections (MIP) for target volume generation in 4DCT scans for lung cancer. *International Journal of Radiation Oncology Biology Physics*, 63(1):253–260, 2005.

[25] J. Wallis and T. Miller. Three-Dimensional Display in Nuclear Medicine and Radiology. *The Journal of Nuclear Medicine*, pages 534–546, 1991.

[26] G. Yan, J. Tian, S. Zhu, Y. Dai, and C. Qin. Fast cone-beam CT image reconstruction using GPU hardware. *Journal of X-ray Science and Technology*, 16(4):225–234, 2008.

[27] Q. Zhang, R. Eagleson, and T. M. Peters. Volume visualization: a technical overview with a focus on medical applications. *Journal of digital imaging*, 24(4):640–664, 2011.

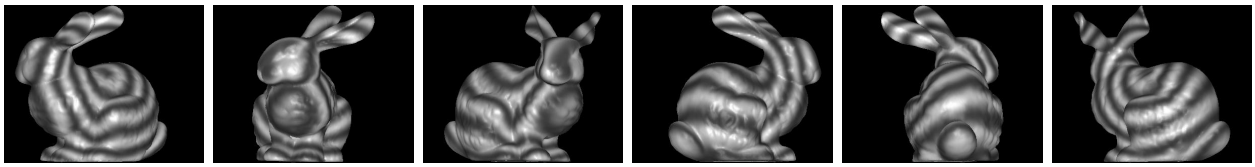

Figure 3: A few images of the sequence for the full example; step of 60 degrees.

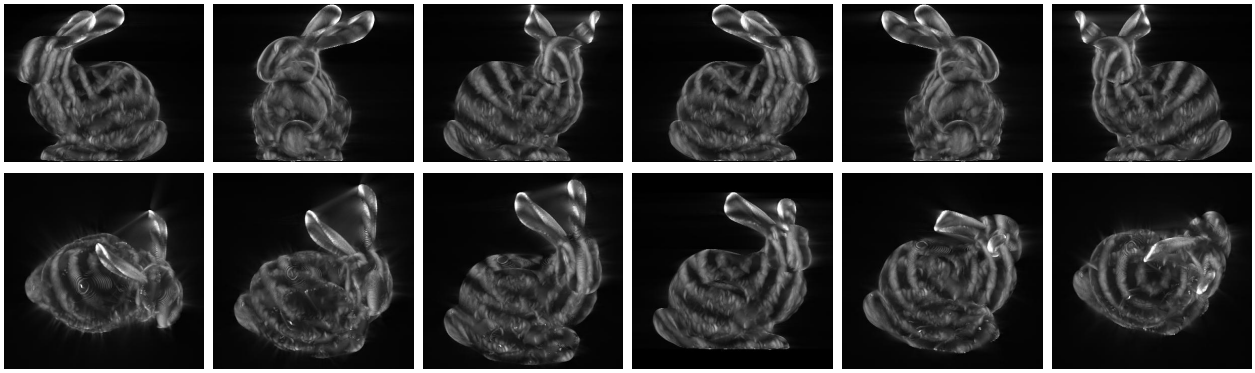

Figure 4: Two sequences of views, computed by the heuristic. Rotation by step of 60 degrees around the vertical axis (first line), and by step of 30 degrees around a horizontal axis (second line).

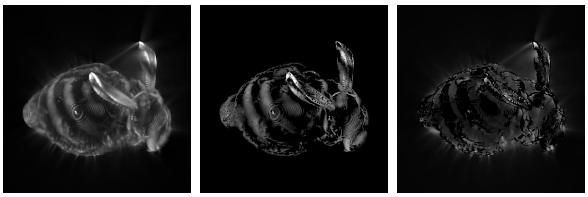

Figure 5: From the left to the right: image I computed by the heuristic, I after selection of the surfacic pixels, I after selection of the non-surfacic pixels.

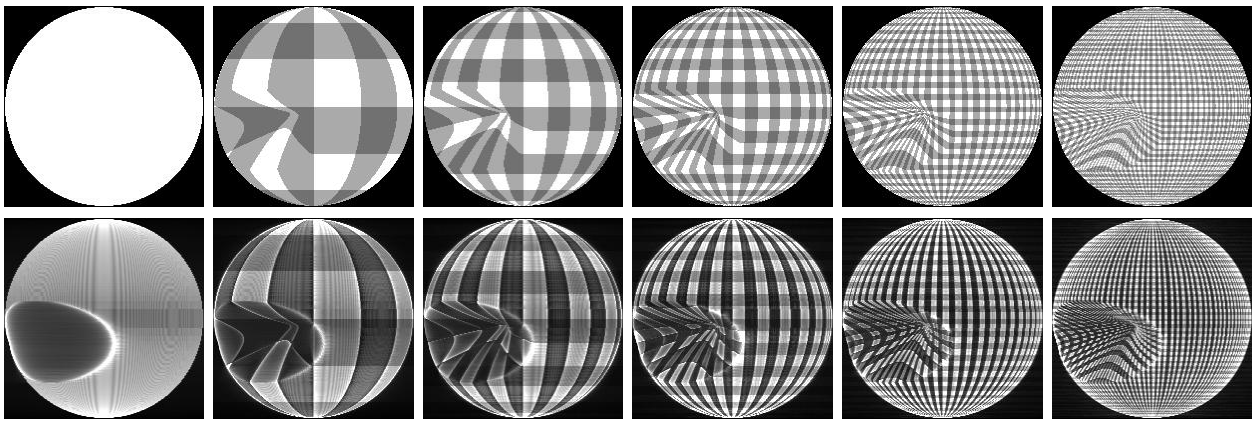

Figure 6: Effect of jumps for a sphere with a dent. From the left to the right: the projected pattern has more and more discontinuities, $m = 0, 2^i, 0 \leqslant i \leqslant 4$. On the first line: one image of the reflectogram; on the second line: associated heuristical reconstruction.

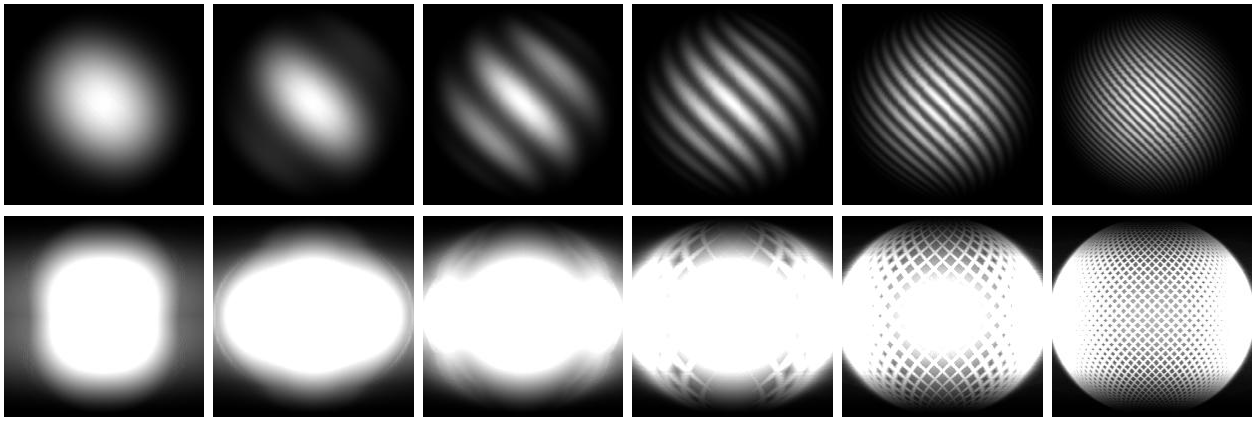

Figure 7: Effect of smooth variations for a sphere. From the left to the right: the frequency parameter is larger and larger: $m = 2^i, 1 \leqslant i \leqslant 6$. On the first line: one image of the reflectogram; on the second line: associated heuristical reconstruction.

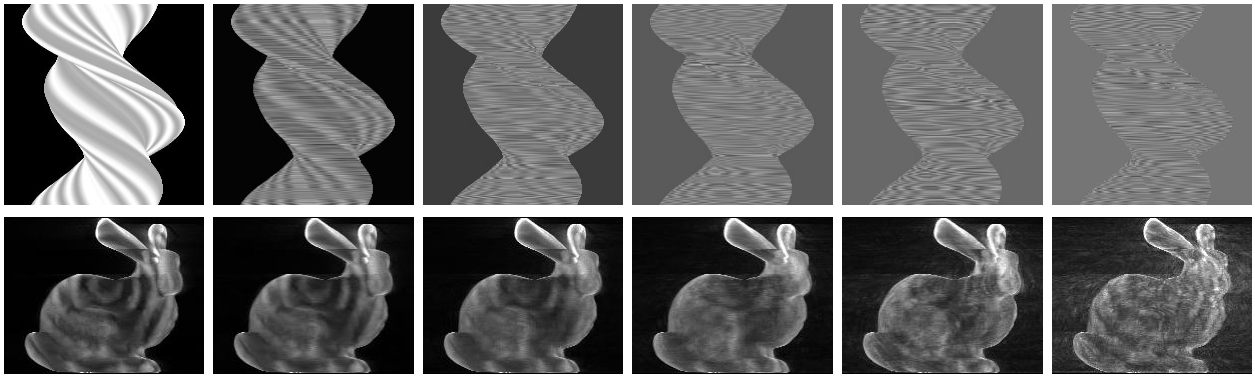

Figure 8: Test of robustness: from the left to the right, the level of disturbance is $\sigma = 0, 2^j, -2 \leqslant j \leqslant 2$. On the first line, slice in the reflectograms: $(\theta, y_2) \mapsto F_\sigma(\theta, y_2, 0)$. On the second line: a vertical view computed by the heuristic.

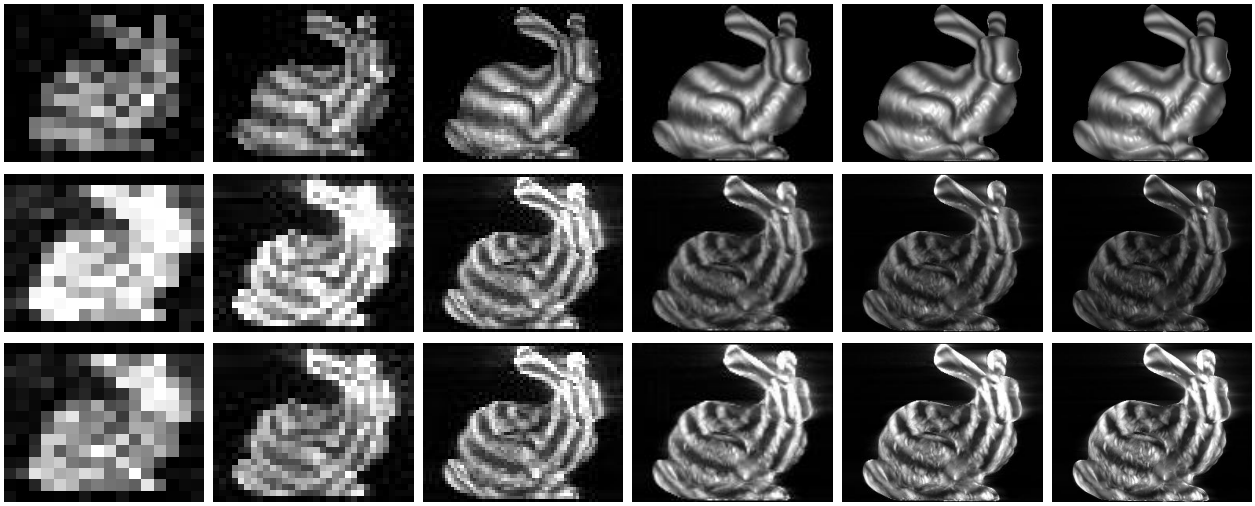

Figure 9: Test of resolution: from the left to the right, the length of an input image is: $N_2 = 16, 32, 64, 128, 256, 384$ (pixels). On the first line, one image of the reflectogram; on the other lines, associated reconstructions with different upper thresholds: $T = 0.5 \max(J_V)$ (second line) and $T_2 = \text{quantile}(\max(J_V, 0), 0.97)$ (third line).

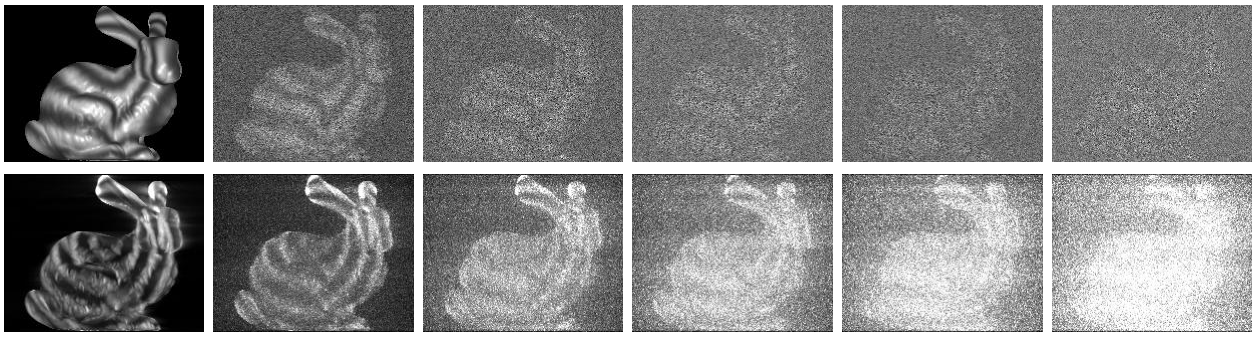

Figure 10: Test of stability. From the left to the right: the level of speckle noise increases: $\sigma = 0.3i, 0 \leqslant i \leqslant 5$. On the first line: one image of the reflectogram; on the second line: associated heuristical reconstruction.

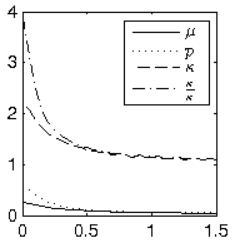

Figure 11: Test of stability: criterions as functions of the level of noise σ.

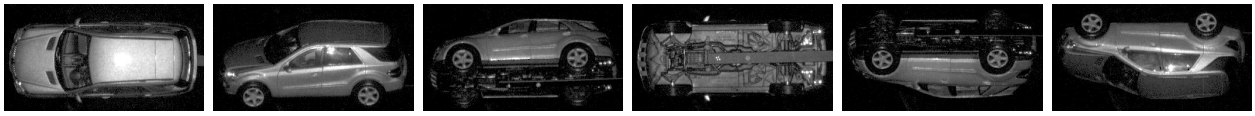

Figure 12: A few images of a sequence of real optronic images; step of 60 degrees.

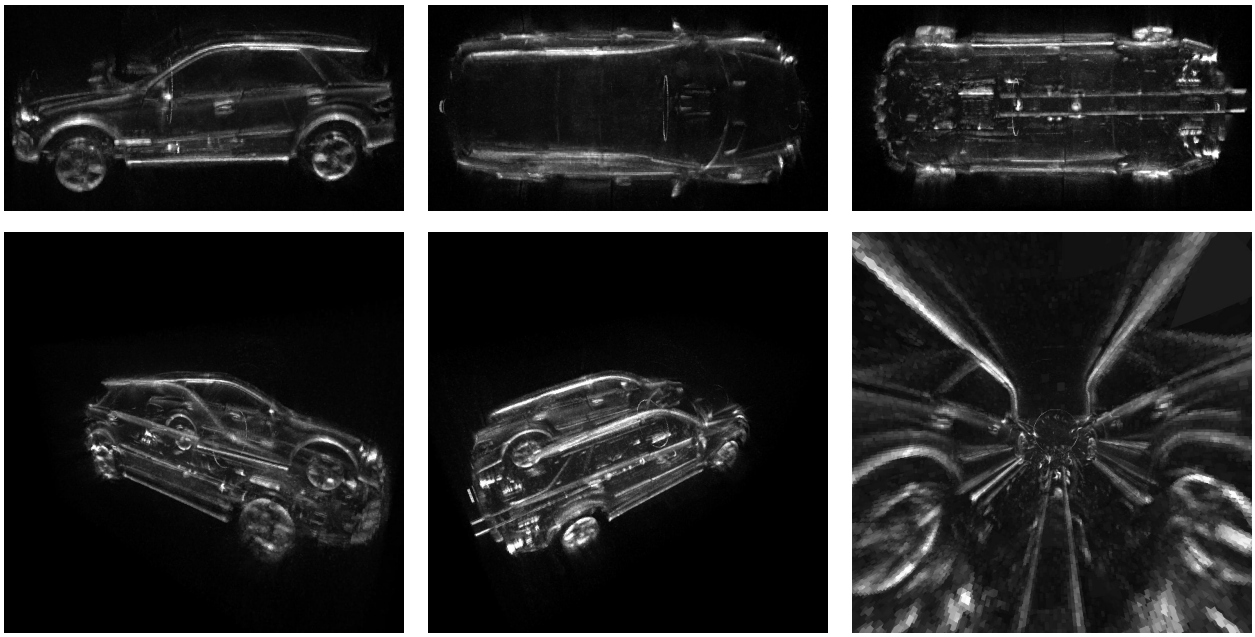

Figure 13: Example of computed views, from the real dataset.